Experimental validation of the vectorial complex ray model on the inter-caustics scattering of oblate droplets

Fabrice R. A. Onofri, Kuan Fang Ren, Matthias Sentis, Quentin Gaubert, Chantal Pelcé

Experimental validation of the vectorial complex ray model on the inter-caustics scattering of oblate droplets

Fabrice R. A. Onofri,[1,*] Kuan Fang Ren,[2] Matthias Sentis,[1] Quentin Gaubert,[1,3] and Chantal Pelcé[1]

[1]*Aix-Marseille Université, CNRS, IUSTI, UMR 7343, 13453, Marseille, France*
[2]*CORIA-UMR 6614, Normandie Université, CNRS, Université et INSA de Rouen, Av de l'Université, BP 12, 76801 Saint Etienne du Rouvray, France*
[3]*IFP Energies nouvelles - Lyon, Rond-point de l'échangeur de Solaize, 69360, Solaize, France*
[*]*fabrice.onofri@univ-amu.fr*

Abstract: We report the first experimental validation of the Vectorial Complex Ray Model (VCRM) using the scattering patterns of large oblate droplets trapped in an acoustic field. The two principal radii and refractive index of the droplets are retrieved with a minimization method that involves VCRM predictions and experimental light scattering patterns. The latter are recorded in the droplet equatorial plane between the primary rainbow region and the associated hyperbolic-umbilic diffraction catastrophe. The results demonstrate that the VCRM can predict the fine and coarse stuctures of scattering patterns with good precision, opening up perspectives for the characterization of large non-spherical particles.

OCIS codes: (290.5850) Scattering, particles; (120.5820) Scattering measurements; (080.1753) Computation methods; (280.2490) Flow diagnostics; (120.6780) Temperature.

References and links

1. K. F. Ren, F. Onofri, C. Rozé, and T. Girasole, "Vectorial complex ray model and application to two-dimensional scattering of plane wave by a spheroidal particle," Opt. Lett. **36**(3), 370–372 (2011).
2. K. Jiang, X. Han, and K. F. Ren, "Scattering of a Gaussian beam by an elliptical cylinder using the vectorial complex ray model," J. Opt. Soc. Am. A **30**(8), 1548–1556 (2013).
3. M. Yang, Y. Wu, X. Sheng, and K. F. Ren, "Comparison of scattering diagrams of large non-spherical particles calculated by VCRM and MLFMA," J. Quant. Spectrosc. Radiat. Transf. in press.
4. H. C. van de Hulst, *Light Scattering by Small Particles* (Dover Publications, 1957).
5. E. A. Hovenac and J. A. Lock, "Assessing the contribution of surface waves and complex rays to far-field scattering by use of the Debye series," J. Opt. Soc. Am. A **9**(5), 781–795 (1992).
6. M. V. Berry, J. F. Nye, and F. J. Wright, "The Elliptic Umbilic Diffraction Catastrophe," Philos. Trans. R. Soc. Lond. A **291**(1382), 453–484 (1979).
7. P. L. Marston and E. H. Trinh, "Hyperbolic umbilic diffraction catastrophe and rainbow scattering from spheroidal drops," Nature **312**(5994), 529–531 (1984).
8. J. F. Nye, "Rainbow scattering from spheroidal drops - an explanation of the hyperbolic umbilic foci," Nature **312**(5994), 531–532 (1984).
9. G. Kaduchak, P. L. Marston, and H. J. Simpson, "E(6) diffraction catastrophe of the primary rainbow of oblate water drops: observations with white-light and laser illumination," Appl. Opt. **33**(21), 4691–4696 (1994).
10. P. L. Marston and G. Kaduchak, "Generalized rainbows and unfolded glories of oblate drops: organization for multiple internal reflections and extension of cusps into Alexander's dark band," Appl. Opt. **33**(21), 4702–4713 (1994).
11. C. E. Dean and P. L. Marston, "Opening rate of the transverse cusp diffraction catastrophe in light scattered by oblate spheroidal drops," Appl. Opt. **30**(24), 3443–3451 (1991).
12. H. Yu, F. Xu, and C. Tropea, "Optical caustics associated with the primary rainbow of oblate droplets: simulation and application in non-sphericity measurement," Opt. Express **21**(22), 25761–25771 (2013).
13. H. Yu, F. Xu, and C. Tropea, "Spheroidal droplet measurements based on generalized rainbow patterns," J. Quant. Spectrosc. Radiat. Transf. **126**, 105–112 (2013).
14. A. L. Yarin, G. Brenn, O. Kastner, D. Rensink, and C. Tropea, "Evaporation of acoustically levitated droplets," J. Fluid Mech. **399**, 151–204 (1999).
15. P. L. Marston, "Rainbow phenomena and the detection of nonsphericity in drops," Appl. Opt. **19**(5), 680–685 (1980).

#238061 - $15.00 USD Received 15 Apr 2015; revised 23 May 2015; accepted 26 May 2015; published 5 Jun 2015

16. M. R. Vetrano, J. P. van Beeck, and M. L. Riethmuller, "Generalization of the rainbow Airy theory to nonuniform spheres," Opt. Lett. **30**(6), 658–660 (2005).
17. F. R. A. Onofri, M. A. Krzysiek, S. Barbosa, V. Messager, K. F. Ren, and J. Mroczka, "Near-critical-angle scattering for the characterization of clouds of bubbles: particular effects," Appl. Opt. **50**(30), 5759–5769 (2011).
18. N. Fdida and J.-B. Blaisot, "Drop size distribution measured by imaging: determination of the measurement volume by the calibration of the point spread function," Meas. Sci. Technol. **21**(2), 025501 (2010).
19. G. Derkachov, D. Jakubczyk, M. Woźniak, J. Archer, and M. Kolwas, "High-precision temperature determination of evaporating light-absorbing and non-light-absorbing droplets," J. Phys. Chem. B **118**(43), 12566–12574 (2014).
20. Y. Yuan, K. F. Ren and C. Rozé, "Fraunhofer diffraction of irregular apertures by Heisenberg uncertainty Monte Carlo model" (in press) (2015).
21. F. R. A. Onofri, S. Radev, M. Sentis, and S. Barbosa, "Physical-optics approximation of near-critical-angle scattering by spheroidal bubbles," Opt. Lett. **37**(22), 4780–4782 (2012).

1. Introduction

Recently, the present authors introduced the Vectorial Complex Ray Model (VCRM) to predict the light scattering patterns of large and arbitrary shaped particles with a smooth surface [1–3]. In VCRM a ray possesses not only four properties: direction, polarization, amplitude and phase as in classical ray models [4], but also a new one – wave front curvature which is governed by the wave front equation [1]. Furthermore, the direction and the Fresnel coefficients are all calculated by the wave vector and its components. So it has three advantages. First, it is inherently three-dimensional and easy to be implemented. Second, the divergence or convergence of the wave on the particle surface and the phase-shifts due to the focal lines can be counted easily. Third, the interference of all rays is taken into account in the VCRM to ultimately obtain the fine and coarse structures of the scattering patterns. Numerical comparisons with the Lorenz-Mie Theory (LMT) were found to be almost perfect for large spheres and cylinders [1, 2], except in the immediate vicinity of classical singularity angles (rainbow, critical angle,...) and where the contributions of surface waves become significant [5]. For spheroids, a fairly good agreement was found with the rigorous electromagnetic models [3]. However, because all current electromagnetic models are still limited to particles of moderate size parameters (less than 600), experimental data are needed to further validate the VCRM.

The goal of this paper is to report the first experimental validation of the VCRM when analyzing the far-field scattering patterns of oblate droplets trapped in an acoustic field. Because current numerical implementation of the VCRM only addresses rays propagating within a droplet's equatorial plane, our analysis is focused on the corresponding scattering plane and, more specifically, in the angular region between the first 'fringe' of the primary rainbow (fold caustic) and first 'fringe' of the caustic associated to the hyperbolic-umbilic diffraction catastrophe (HDUC) [6–10]. In this angular region, hereafter referred to as the inter-caustics region, classical geometrical ray-models for oblate droplets [7–13] can only predict the skeleton of the caustics, while as it is shown, the VCRM allows for predicting, with high computational efficiency and accuracy, the coarse and fine structures of the scattering patterns.

3. Experimental setup

The whole experiment is built around an ultrasonic levitator operating at 100 kHz (Fig. 1). The droplet under study is trapped slightly below the pressure nodes, between the ultrasound emitter and reflector. Due to the symmetry of the system, the droplet is assumed to be oblate. Its vertical principal radius b, along the gravity direction, is smaller than its horizontal principal radii a and c, i.e., $c = a$ with $b/a<1$. Basically, the higher the amplitude of the acoustic field, the lower the droplet aspect ratio b/a [14].

The measurement setup is first composed of a Rainbow Diffractometry (RD) system (also called a Rainbow interferometer [15] or refractometer [16]). The emitting optics of the RD-system illuminate the droplet along the z-axis with a large, collimated, perpendicular polarized, coherent and continuous laser beam with wavelength λ = 532.130 nm and local waist radius w_0 = 5.5 mm, with $w_0/a>>1$. The perpendicular polarization, i.e., the incident

#238061 - $15.00 USD Received 15 Apr 2015; revised 23 May 2015; accepted 26 May 2015; published 5 Jun 2015

wave vector **k** and electrical field **E** are both in the *yz*-plane, provides rainbow fringes with highest contrast. The high coherence length (50 m) and high laser power (2 W) of the laser source, as well as the limited exposure time of the CCD camera (35 µs, see later on), are required to obtain both the fine and coarse structures of the scattering (and not only the so-called "global" structures [11–13]). The detection of the RD-system records the droplet far-field scattering pattern in the inter-caustics region in the vicinity of the droplet equatorial plane (*xz*-plane in Fig. 1). This detection system is almost identical to the one developed for the study of critical scattering [17]. It is composed of a collection optics that image the droplet in the plane of an iris diaphragm and an achromatic doublet that performs the Fourier transform of the previously spatially filtered signal onto the chip of a high resolution CCD camera (4 Mpix, 14 bits). The angular resolution of the RD-system is $\delta\theta \approx 0.02°$/pixel for a maximum angular field of view of $\Delta\theta \approx 29°$.

A shadowgraph imaging (SI) system is used for the comparison of size measurements. Its emission optics backlight the droplet by producing a band-pass, pulsed and collimated beam (flash duration of 5 µs). The detection of the SI-system is simply composed of a pass-band filter, a double telecentric video lens and a CCD camera identical to, and synchronized with, that of the RD-system. The SI-system's micrometer to pixel calibration factor is 0.674 pix/µm. Classically, the droplet diameter is obtained from its normalized contrast function and a sub-pixel interpolation scheme [18].

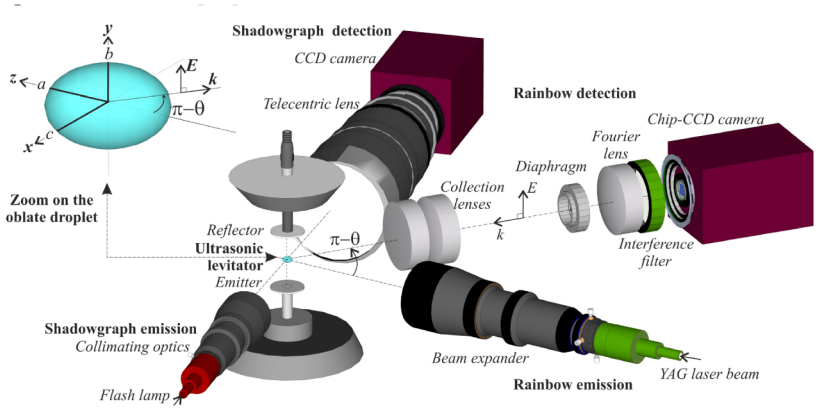

Fig. 1. Experimental setup with coordinate system.

Experiments are performed on a single droplet of Di-Ethyl-Hexyl-Sebacat (DEHS, provided by Topas GmbH), whose characteristics are monitored when the amplitude of the acoustic field is decreased continuously from 156 dB to 148 dB in 60 seconds (i.e., maximum recording time for both optical systems). DEHS is commonly used for fluid-flow characterization as a non-soluble (i.e., not sensitive to atmospheric moisture), colorless (the imaginary part of refractive index is estimated to be of less than $k = 10^{-6}$) and non-toxic liquid. Simple considerations demonstrate that the droplet temperature increase due to the laser heating is of less than $5\ 10^{-4}$°C during the course of an experiment. Due to DEHS's low vapor pressure, we expect the volume of the droplet to be fairly constant during the course of the experiment. This is a major *the droplet temperature increases* difference with experiments carried with micron-sized [19] or millimeter-sized water droplets, e.g [13, 15]. For the same reason and due to the heating induced by the acoustic trap, the temperature of the DEHS droplet is expected to increase during the course of the experiment and, thus, its refractive index will decrease. DEHS refractive index variation with temperature was measured to be $-3.87\ 10^{-4}$/C° for our operating conditions.

#238061 - $15.00 USD Received 15 Apr 2015; revised 23 May 2015; accepted 26 May 2015; published 5 Jun 2015

3. Comparison method and parameter estimation

On a desktop computer, the VCRM takes only a few hundred milliseconds to calculate the whole scattering pattern of large spheroidal droplets (e.g., approximately 2800 in what follows). However, because the fine structure of the scattering patterns is extremely sensitive to the droplet parameters (principal radii and refractive index) [15], it is necessary to calculate millions of scattering diagrams to retrieve these parameters when comparing experimental and numerical scattering patterns. To do so, our strategy is to pre-calculate and store the VCRM calculations in a four-dimensional look-up table. The latter contains $N_\theta \times N_a \times N_b \times N_m$ elements $S_{i,\alpha,\beta,\mu}$ representing the far-field intensity in the equatorial plane and direction θ_i, with $i = 1, 2,..., N_\theta$, that is scattered by a droplet of horizontal principal radius a_α, with $\alpha = 1, 2,..., N_a$, vertical principal radius b_β, with $\beta = 1, 2,...,N_b$, and real refractive index m_μ, with $\mu = 1, 2,..., N_m$. To retrieve the droplet parameters, a simple unconstrained least-square minimization of the function ε is performed:

$$(a,b,m) \equiv \left\{ \left(a_\alpha, b_\beta, m_\mu\right) / \min_{a_\alpha b_\beta, m_\mu} (\varepsilon) \right\} \text{ with } \varepsilon\left(a_\alpha, b_\beta, m_\mu\right) = \sum_{i=v}^{i=w} \left(S'_{i,\alpha,\beta,\mu} - E'_i\right)^2 \quad (1)$$

where $S'_{i,\alpha,\beta,\mu}$ is the normalized intensity calculated with the VCRM and E'_i is the interpolated value of the measured signal at θ_i and after normalization. For given values of a_α, b_β and m_μ, the VCRM and experimental scattered intensities are normalized in the same angular range, θ_v, θ_{v+1},…, θ_w, with $v \geq 1$ and $w \leq N_\theta$:

$$S'_{i,\alpha,\beta,\mu} = S_{i,\alpha,\beta,\mu} \Big/ \sum_{i=v}^{i=w} S_{i,\alpha,\beta,\mu}\,,\; E'_i = E_i \Big/ \sum_{i=v}^{i=w} E_i\,. \quad (2)$$

For best performance, the angular range used for the normalization and minimization function should be dependent on the droplet's properties, i.e., $v \equiv v(a_\alpha, b_\beta, m_\mu)$ and $w \equiv w(a_\alpha, b_\beta, m_\mu)$, because the angular width of the inter-caustic region depends on these parameters, as shown in Fig. 2. However, in the present work, to simplify, the same reduced angular range is used for all droplets. For all calculations reported below, we have $N_\theta = 600$, $N_a = N_b = 251$ and $N_m = 125$, corresponding to the droplet's radii and refractive index increments of 50 nm and 4×10^{-4}, respectively. After a first estimation of the droplet parameters, iterative calculations are performed to achieve a resolution of 10 nm and 1×10^{-4}. The VCRM calculations are limited to the first eight scattering orders ($p = 0, 1,..., 7$) [1–4].

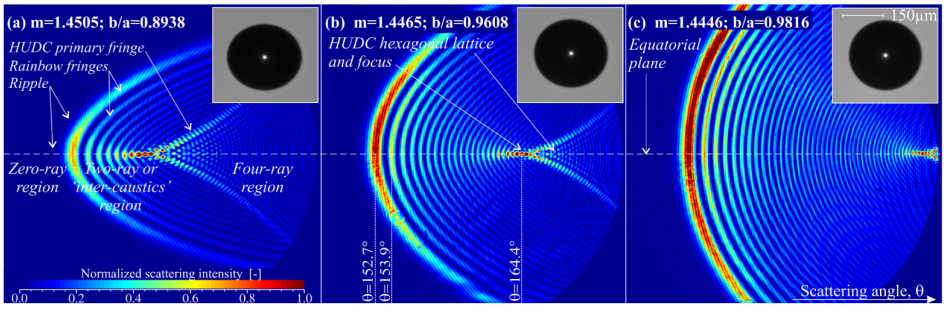

Fig. 2. Experimental far-field scattering patterns (color coding: intensity) and shadowgraph images (top right corners) of a DEHS droplet. From (a) to (c), the droplet's aspect ratio *b/a* increases and refractive index decreases when the amplitude of the acoustic field is reduced.

4. Results and discussion

Typical scattering patterns and shadowgraph images are shown in Fig. 2(a-c) for a droplet with an aspect ratio *b/a* that increases from 0.8938 up to 0.9816. Clearly, the shadowgraph images justify our hypothesis that, for our operating conditions, the droplet is oblate. In the

#238061 - $15.00 USD Received 15 Apr 2015; revised 23 May 2015; accepted 26 May 2015; published 5 Jun 2015

far-field scattering patterns, two rather unusual trends emerge when compared to the spherical case: the elliptical curvature of the primary rainbow fringe and the complex pattern associated to the HUDC [6–8]. As observed earlier [7,8], the latter seems to originate from the backward direction ($\theta = 180°$) and move towards the primary rainbow fringe for decreasing aspect ratios. From Fig. 2(a), it is obvious that the structure of the HUDC pattern (cusp edge, focus, hexagonal lattice structure,...) [6, 9] is indeed more complex than observed in the time-averaged scattering patterns (e.g., [11–13]). By extracting the equatorial intensity profiles from Fig. 2(a-c) and using the minimization method introduced above, with $\theta_v = 152.3°$ and $\theta_w = 157.3°$, we compare the experimental and numerical intensity profiles in Fig. 3(a-d). The first conclusion is rather straightforward. Within experimental uncertainties (e.g., CCD dark noise and residual non-linearity, calibration errors, optical aberrations,...), the VCRM predictions fit the experimental scattering patterns in the inter-caustic region very well. The agreement is more qualitative in the immediate vicinity of the aforementioned diffraction catastrophes (rainbow and HUDC), as well in the backward scattering region. The reasons for this are clear. According to Marston and Trinh [7], as well as Nye's [8] terminology, the current VCRM calculations are expected to be valid only in the 'zero-ray region' (i.e., Alexander's dark band, where there is no contribution from $p = 2$ rays) and the 'two-ray region' (i.e., the inter-caustics region, where two $p = 2$ rays propagating in the droplet equatorial plane are responsible for the rainbow phenomena, see Fig. 2(a)). The same holds true for the "four-rays" region, where the complex scattering pattern is mainly attributed to the contributions of two $p = 2$ rays propagating in the droplet equatorial plane and two skew $p = 2$ rays propagating above and below the droplet equatorial plane (for more details, see Fig. 5 in [7]).

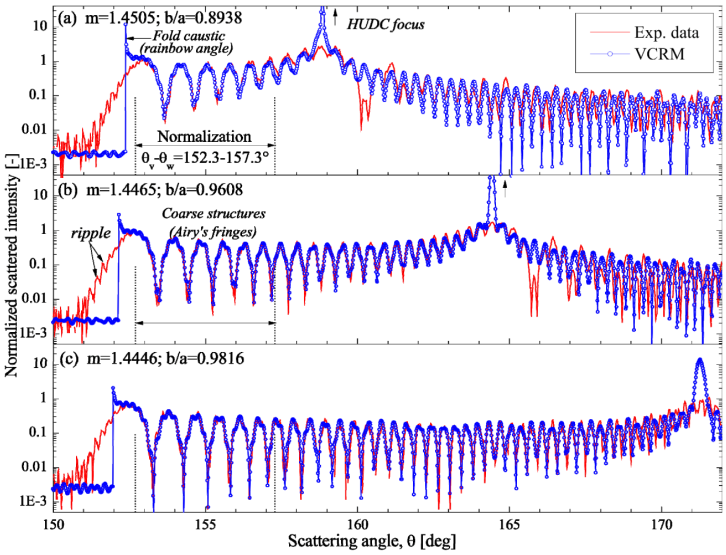

Fig. 3. Comparison of VCRM and experimental normalized equatorial scattering diagrams for the droplets considered in Fig. 2.

The evolutions of the principal radii obtained with the SI- and RD-systems during the course of the experiment are compared in Fig. 4(a). Note that, for drawing considerations, the uncertainty on shadowgraph measurements (± 1.5 µm) is shown as dashed lines rather than error bars. Here, we clearly experience the predictive power of the VCRM. The average differences between the two time series of Fig. 4(a) are only 0.05 µm, –0.09 µm and –0.001 for *a*, *b* and *b/a*, respectively, and 0.17 µm, 0.35 µm and 0.003 for the corresponding root-mean-square-differences. It may be surprising that the principal radii of oblate droplets can be inferred so accurately in a plane where their cross section is circular. However, this can be easily understood by recalling two points. First, in the VCRM, a curvature matrix of the local

#238061 - $15.00 USD Received 15 Apr 2015; revised 23 May 2015; accepted 26 May 2015; published 5 Jun 2015

wave front is associated to each ray so that rays propagating in the equatorial plane do carry information on a and b [1]. Second, it has long been known that even the fine structure of the scattering diagrams of a sphere and right circular cylinder (with the same radius) exhibit differences due to the particle surface curvature in the direction perpendicular to the equatorial plane. Figure 4 (b) shows that the droplet refractive index decreases significantly during the course of the experiment, while its spherical equivalent diameter remains almost constant, $R_{Sph} = (ba^2)^{1/3} \approx 137.47 \pm 0.21$ µm. This behavior, which will be detailed in a future work, is simply attributed to the heating induced by the acoustic trap and low evaporation rate of DEHS. These results justify also a posteriori our implicit assumption that internal refractive index gradients are (partly) negligible. This may be understood by the rotation of the droplets in the trap, both horizontally and vertically, and that the acoustic field generates vortices in the surrounding air [14]. All these effects induce strong and complex internal recirculations (easily observable with seeding particles) of the fluid inside the droplet, homogenizing the temperature of the droplet.

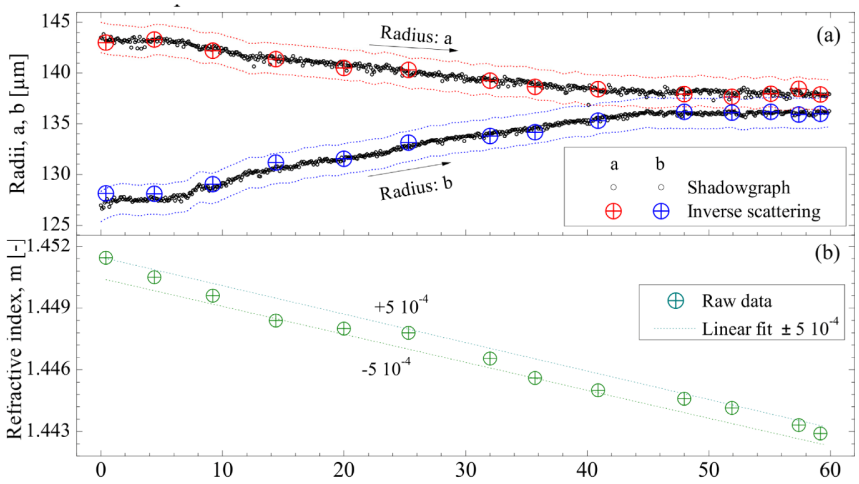

Fig. 4. (a) Principal radii measured with the RD- and SI-System and (b) corresponding evolution of the droplet refractive index during the course of the experiment.

5. Conclusions and perspectives

The VRCM predictions fit well the experimental scattering patterns of large oblate droplets trapped in an acoustic field. The VCRM accuracy, with its high computational efficiency, has permitted the retrieval of the evolution of the two principal radii and refractive index of slow evaporating droplets. To further extend the capabilities of this model, particularly in the immediate vicinity of caustics, physical optics approximations must be included. Although not discussed in this paper, this has already been performed using Heisenberg's principle [20] for the forward diffraction of spheroid particles, and an important preliminary step has been achieved for the near-critical-angle scattering of spheroid bubbles [21]. A similar and even more challenging work has to be performed for notably the diffraction catastrophes [6–11]. To do so, it will also be necessary to develop a three-dimensional numerical implementation of the VCRM. The experimental results and trends reported in this study are necessary ingredients for the validation of these next steps. They also clearly demonstrate that to monitor the properties of large droplets, their non-sphericity must be considered.

Acknowledgments

This work was partially funded by the French National Research Agency (ANR) under grants AMO-COPS (ANR-13-BS09-0008-01, ANR-13-BS09-0008-02), Labex MEC (ANR-11-LABX-0092) and A*MIDEX (ANR-11-IDEX-0001-0).

#238061 - $15.00 USD Received 15 Apr 2015; revised 23 May 2015; accepted 26 May 2015; published 5 Jun 2015